

Simulation-Based Feasibility Analysis of Ship Detection Using GNSS-R Delay-Doppler Maps

Tiziana Beltramonte, Paolo Braca , *Senior Member, IEEE*, Maurizio Di Bisceglie , *Member, IEEE*, Alessio Di Simone , *Member, IEEE*, Carmela Galdi , *Member, IEEE*, Antonio Iodice , *Senior Member, IEEE*, Leonardo M. Millefiori , *Member, IEEE*, Daniele Riccio , *Fellow, IEEE*, and Peter Willett , *Fellow, IEEE*

Abstract—In this article, we carry out a simulation analysis of ship detection via Global Navigation Satellite System-Reflectometry (GNSS-R) delay-Doppler map (DDM). The GNSS-R DDM simulator used here is a modified version of an algorithm conceived for the generation of GNSS-R DDMs of the sea surface. The new algorithm is based on an analytical model for the radar cross section of ships and is able to properly account for the presence of ship targets within the scene. The proposed GNSS-R DDM simulator is, then, exploited for assessing the viability of GNSS-R in ship detection applications at low incidence angles, where the adopted scattering models provide accurate results. The aim of the implemented simulation setup is to analyze what are the preferable conditions for ship detection using standard GNSS-R signal processing chain receiver and compare typical forward left-hand circularly polarized GNSS-R systems with nonstandard backward right-hand circularly polarized (RHCP) GNSS-R. The simulation study is two fold: first, detection performance is evaluated at spaceborne and airborne altitudes for both polarization channels under favorable detection conditions. Then, visibility of ship targets is assessed in terms of their location within the DDM. Simulation results show that ship detection is problematic when using satellite data, whereas interesting results are achieved at airborne altitudes, provided that the aircraft is approximately between the GNSS satellite and the target, and that appropriate RHCP polarization is probed. In such configurations, signal-to-noise-ratios larger than 10 dB are obtained with airborne receivers collecting the RHCP signal.

Index Terms—Bistatic radar, delay-doppler map (DDM), global navigation satellite system-reflectometry (GNSS-R), GNSS-R simulator, maritime surveillance, radar cross section, ship detection.

Manuscript received July 26, 2019; revised November 5, 2019, December 7, 2019, and January 13, 2020; accepted January 16, 2020. Date of publication March 12, 2020; date of current version April 21, 2020. This work was supported in part by the Office of Naval Research under Contract N00014-16-13157 (this support is acknowledged with thanks to J. Tague and M. Vaccaro) and in part by the ONR-Global. (*Corresponding author: Alessio Di Simone.*)

Tiziana Beltramonte, Maurizio Di Bisceglie, and Carmela Galdi are with the Department of Engineering, University of Sannio, 82100 Benevento, Italy (e-mail: tbeltram@unisannio.it; dibisceg@unisannio.it; galdi@unisannio.it).

Paolo Braca and Leonardo M. Millefiori are with the NATO-STO Centre for Maritime Research and Experimentation, 19126 La Spezia, Italy (e-mail: paolo.braca@cmre.nato.int; leonardo.millefiori@cmre.nato.int).

Alessio Di Simone, Antonio Iodice, and Daniele Riccio are with the Department of Information Technology and Electrical Engineering, University of Napoli Federico II, 80125 Napoli, Italy (e-mail: alessio.disimone@unina.it; iodice@unina.it; daniele.riccio@unina.it).

Peter Willett is with the Department of Electrical and Computer Engineering, University of Connecticut, Storrs, CT 06269 USA (e-mail: peter.willett@uconn.edu).

Digital Object Identifier 10.1109/JSTARS.2020.2970221

I. INTRODUCTION

GLOBAL Navigation Satellite System-Reflectometry (GNSS-R) delay-Doppler maps (DDMs) collected over ocean are typically exploited for the analysis of the sea surface. Few applications have been conceived and assessed so far, namely wind speed retrieval, sea surface roughness, and sea altimetry [1]–[5]. Due to the very low signal-to-noise ratio (SNR) of the received earth-reflected signal, it is of key relevance to properly design the system geometry and the signal processing chain according to the scattering features of the sensed scene. In maritime environments, most electromagnetic (EM) energy impinging upon the ocean surface is scattered within an angular region around the specular reflection direction, whose width depends on the sea surface roughness conditions. In addition, with reference to the Global Positioning System (GPS), the dielectric properties of seawater make the reflected signal generally reverse from the transmitted right-hand circular polarization (RHCP) to the left-hand circular polarization (LHCP) [6], [7]. Accordingly, for sea surface analysis, best performances, i.e., largest SNR values, are achieved with a GNSS-R receiver acquiring the LHCP component of the scattered signal in a forward-scattering configuration (see Fig. 1). Hereafter, we refer to such systems as standard GNSS-R.

Besides sea state observation, GNSS-R observables are experiencing an increasing interest in applications related to the maritime surveillance, where it appears to be a prospective and very attractive solution. Indeed, in contrast with other remote sensing technologies, e.g., synthetic aperture radar (SAR) and multispectral sensors, spaceborne GNSS-R offers worldwide coverage with an unprecedented revisit time down to few hours when operating in constellation formation [8], [9]. The main benefit of GNSS-R comes from the exploitation of GNSS signals of opportunity, which can be properly used for remote sensing applications. With the deployment of the European Galileo and the Chinese BeiDou-2 GNSSs, more than 100 GNSS signals continuously illuminating the earth's surface will be available free of charge. Considering that each GNSS-R receiver can track several GNSS signals at the same time, hundreds of points over the earth's surface may be tracked simultaneously, thereby enabling real-time remote sensing and earth's observation. The chance of exploiting GNSS signals of opportunity makes GNSS-R receivers be carried onboard light-weight, compact, low-energy, and low-cost payloads as opposed to other remote sensing technologies.

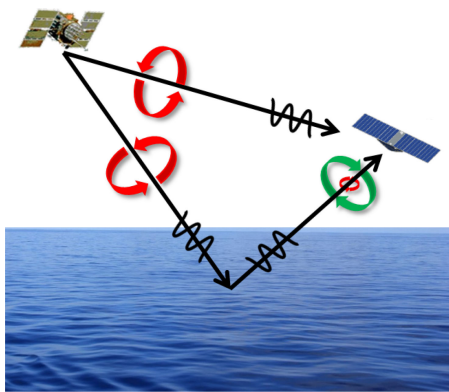


Fig. 1. Ship-free scenario. Signal polarization is represented through red (RHCP) and green (LHCP) circles, whose size is proportional to the polarization component intensity. In the ship-free scenario, the transmitted RHCP signal is scattered in the specular reflection direction and becomes mostly LHCP.

However, investigations in this field are still on an exploratory path and the literature focusing on ship detection using GNSS signals of opportunity is still sparse [9]–[17]. Preliminary analyzes of the GNSS signal reflected from a ship target were first carried out in [12] and [13]. In [12], an experimental airborne campaign was conducted to prove the effectiveness of a hard-thresholding detection algorithm, whereas the work in [13] introduces a new constant false alarm rate method for ship detection using GPS-R correlation power spectra. The works in [14]–[16] discuss the detection and the localization of ship targets by using coastal-based receivers and long integration times. The works in [9] and [11] provide a preliminary study of the ship detection problem using spaceborne GNSS-R DDMs. However, due to the lack of ground-truth data, the presented detector was tested over a sea ice sheet and a large oil platform. Indeed, no detections of actual ship targets were presented therein. Finally, the limits of standard GNSS-R and the potential benefits of the backscattering configuration for ship detection applications were first envisioned in [10], where a link budget analysis under different operating conditions and scenarios was carried out, and tested successfully in [17] by means of an airborne campaign.

From the related literature, it emerges that the applicability of standard GNSS-R to ship detection is mainly impaired by the poor spatial resolution—on the order of few kilometers close to the specular reflection point—and by the very low SNR of the target echo, which makes detectability of ship targets in DDMs still questionable. For the sake of clarity, three TechDemoSat (TDS)-1 DDMs with ship targets are shown in Fig. 2. The DDMs were acquired over the Indian Ocean and comprise four ship targets each (marked with black crosses), whose positions are gathered via satellite automatic identification system data provided by NATO STO CMRE. Ship lengths range from 184 to 333 m in all three cases. Despite the large dimensions, there is no clear evidence of the presence of the ships within the shown DDMs as the disturbance to the reflected signal power due to the presence of the ships is too weak and do not allow for reliable detections.

Several factors are likely to impair ship detectability using GNSS signals of opportunity. First, the GNSSs provide a very low power density, which can be as low as $3 \times 10^{-14} \text{ W/m}^2$ at

the earth's surface [18], thus motivating a strong thermal noise reduction performed onboard GNSS-R receiver through temporal multilook, i.e., incoherent integration of single-snapshot DDMs. However, the power transmitted by GNSS stations has to be considered an environment parameter in the sense that it is fixed and cannot be changed according to the end-user requirements.

Besides the GNSS power density issue, the poor detection capabilities of current GNSS-R may be partly justified by the fact that the operating conditions of standard systems are not suited to ship detection applications. Indeed, the EM energy impinging over the ship undergoes both single- and multiple-bounce phenomena between the ship hull and the sea surface (see Fig. 3) as opposed to the ship-free scenario, where the received signal is due to the single-bounce scattering from the sea surface only (see Fig. 1). Multiple-bounce contributions enhance the energy backscattered from the ship, whereas the single-bounce term dominates the energy reflected by the ship in the specular direction. However, such a contribution, despite its relative strength, is very hardly detectable, as it requires the specular reflection point falling within the ship deck area. In addition, in the conventional forward geometry, it might be challenging to distinguish the return from the ship deck from the signal reflected off a very calm sea surface.

Moreover, the metallic hull of the ship reverses the polarization of the impinging EM wave. Accordingly, it is reasonable to expect that the double scattering contribution exhibits a non-negligible RHCP component, same as the transmitted waveform. Unfortunately, at the best of the authors' knowledge, the literature related to the bistatic scattering from ships and taking into account the coupling effects with the surrounding sea surface in circular polarization is sparse. Notwithstanding, valid support is provided by the theoretical link budget analyzes in [19] and [20], where the RCS of the ship is modeled according to [21].

In addition, it is worth mentioning that the presence of metallic structures on the deck—masts, control rooms, isolated containers, etc.—would cause a raise in the LHCP component of the signal backscattered from the ship due to odd-bounces contributions between such structures. To better investigate the chance of exploiting these signals for ship detection applications, we here recall that the RCS of a trihedral corner reflector with a size on the order of meters exhibits an RCS of $10^2 - 10^3 \text{ m}^2$ in *L*-band (see [22]). Conversely, the backscattering RCS of a sea surface area on the order of few hundred meters (typical value in GNSS-R) results in an RCS value on the order of $10^5 - 10^6 \text{ m}^2$ (see [23]). Accordingly, such triple-bounce contributions are expected to have a negligible impact on the received LHCP signal and are likely to not represent a reliable source for detecting ships using the LHCP receiving channel in a backscattering configuration.

In conclusion, for sea surface analysis (ship-free scenario), the received signal is mostly LHCP and comes from a region surrounding the specular reflection point, the so-called glistening zone. Conversely, for ship detection applications (ship scenario), the signal emerging from the target is mostly RHCP and is reflected in a direction far away the specular reflection direction. Such physical-driven considerations are confirmed by the link

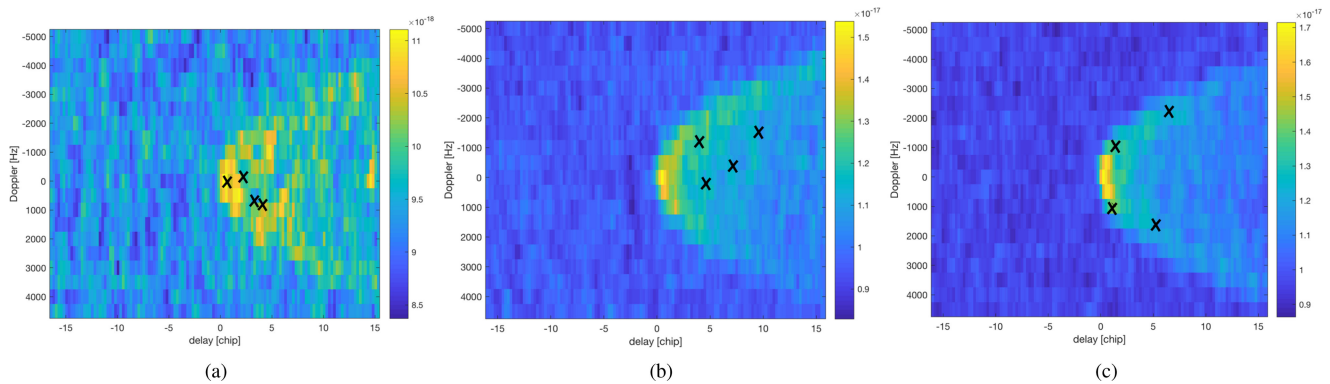


Fig. 2. TDS-1 DDMs comprising four targets each (marked through black crosses) and acquired over the Arabian Sea on (a) Feb. 4, 2015 at 17:33:19, (b) Apr. 17, 2015 at 06:01:48, and (c) Apr. 17, 2015 at 06:03:49.

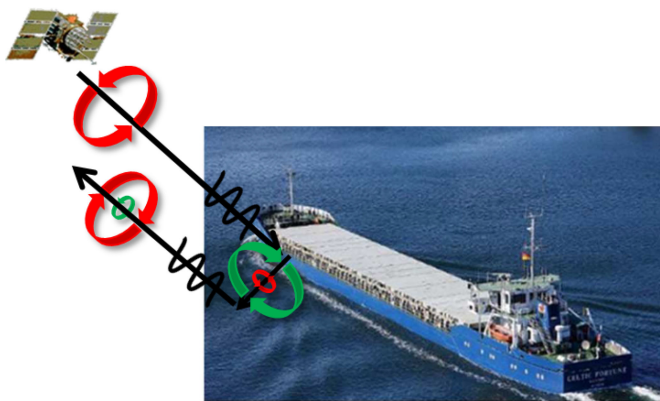


Fig. 3. Scenario comprising a ship target. Signal polarization is represented through red (RHCP) and green (LHCP) circles, whose size is proportional to the polarization component intensity. As opposed to the ship-free scenario, the signal scattered from the ship target is reflected back towards the transmitter after a double-bounce reflection. Both reflections mostly change the polarization of the signal that then is predominantly RHCP again.

budget analyzes conducted in [19], [20], and [24], where the feasibility of the ship detection problem was conducted on a theoretical basis by evaluating the SNR and the signal-to-noise-plus-clutter ratio (SNCR) in different operating conditions. In those works, it was demonstrated that even large ships are scarcely detectable with standard spaceborne GNSS-R, as SNCR and SNR values well below zero were obtained. Moreover, the benefits of nonstandard backward-RHCP GNSS-R—GNSS-R receivers specifically designed for ship detection applications acquiring the RHCP component of the backscattered signal—were envisaged. The theoretical link budget analyzes in [19], [20], and [24] provide useful insights for a preliminary understanding of ship detectability using GNSS-R. Based on accurate scattering models, they enable a fast and reliable assessment of the expected ship detection performance under different operating conditions and scenarios providing meaningful guidelines for the design of GNSS-R systems properly designed for maritime surveillance applications. However, such theoretical analyzes do not enable a full understanding of the detection problem, as a number of effects cannot be easily accounted for. Just for example, the link budget in [19], [20], and [24] does not take

into account for the effects of the Woodward ambiguity function (WAF) and speckle noise. Accordingly, to better understand the role of such additional effects on ship detectability and address a more accurate analysis of the expected detection performance, it is of key relevance to rely on more accurate tools.

In this work, we carry out a feasibility analysis of ship detection using GNSS-R DDMs by means of simulation tools. The aim of such an analysis is two-fold: 1) to account for those additional effects related to speckle noise and WAF that were neglected in related works; 2) to expand previous analyzes to airborne configurations and to assess the role of the receiver altitude and target location on detection performance. The simulator adopted is based on analytical EM scattering models for both the sea surface and the ship target. However, such models are not accurate at large incidence angles as they are both derived in the framework of the Kirchhoff approximation (KA)-geometrical optics (GO). Accordingly, here, we limit our analysis to low incidence angles.

The rest of this work is organized as follows. Section II briefly introduces the radar cross section (RCS) model of the ship target, whereas Section III presents the GNSS-R DDMs simulator. Results of the simulation study are shown and discussed in Section IV. Finally, conclusions are drawn in Section V.

II. ELECTROMAGNETIC SCATTERING MODEL FOR THE SHIP TARGET

In this Section, we briefly introduce the RCS model for the ship target adopted within the GNSS-R simulation algorithm. Here, we focus on scenarios similar to that shown in Fig. 3, which comprises an isolated large and slowly-moving ship. The EM characterization of the ship target is, here, made according to the work in [21], which generalizes the analytical backscattering model developed in [25] to the more generic bistatic case. In [21], the far-field EM field scattered from a canonical isolated ship is analytically derived under the KA-GO and by accounting for the mutual interactions between the ship body and the surrounding sea surface. For mathematical tractability of the scattering problem, a simplified geometry is assumed for the maritime environment. In particular, the ship is modeled as a parallelepiped with smooth faces, whereas the

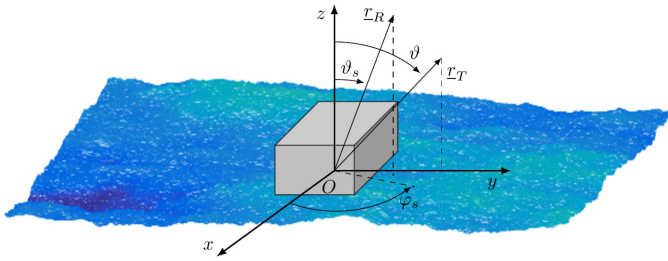


Fig. 4. Coordinate system for the scattering problem.

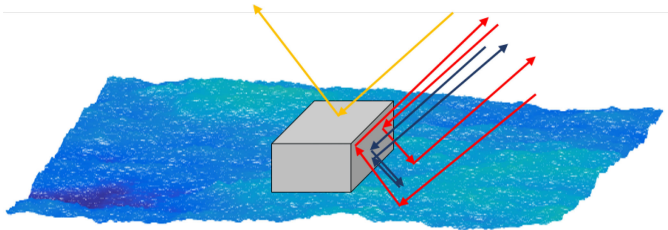


Fig. 5. Geometry of the scattering problem for the ship target. Scattering contributions are highlighted as concatenated arrows. Single-bounce (yellow lines), double-bounce (red lines), and triple-bounce (dark blue lines) contributions.

ocean surface roughness is described as an infinite 2-D isotropic normally-distributed process and wind speed-dependent variance. In addition, a uniform illumination is assumed over the surface area contributing to ship scattering, i.e., the incident field is described as a plane wave.

The coordinate system for RCS evaluation is shown in Fig. 4 and is defined according to [21] and [25], i.e., the xy plane coincides with the sea surface mean plane, whereas the origin of the reference system is, here, chosen such that the center of the target is at $(0, 0, h/2)$, h being the ship height. The transmitting GNSS station lies in the $(z > 0, y > 0)$ quadrant and is, therefore, defined only by the transmitter look angle ϑ ; the receiver has look angle ϑ_s and azimuth angle φ_s . The EM scattering phenomena are illustrated in Fig. 5. Under GO, the field scattered from the ship is decomposed as the superposition of different terms arising from the coupling between the ship hull and the sea surface [21] as follows:

- 1) one single-bounce contribution from the ship deck;
- 2) two double-bounce contributions (hull-sea and sea-hull);
- 3) one triple-bounce contribution (hull-sea-hull).

All the bounces are highlighted in Fig. 5 as concatenated arrows. As the ship faces are assumed smooth and the operating wavelength is much smaller than the ship dimensions, the single-bounce term is non-negligible only in a very narrow angular region around the specular reflection direction. It is also interesting to note that the scattering from the ship deck is a ray-optics reflection only as long as the deck is larger than (at least) the first Fresnel zone. In our cases, this assumption is not valid and the scattering deck surface, despite being smooth, behaves like a (deterministic) diffuse scatterer, due to diffraction. This is a result not only of the scattering model adopted here, but also of any model employed to compute the RCS of a flat metallic plate (see, e.g., [26]). The double-bounce scattering terms are characterized by a double reflection on the ship hull and sea surface (see red lines in Fig. 5): the hull-sea contribution

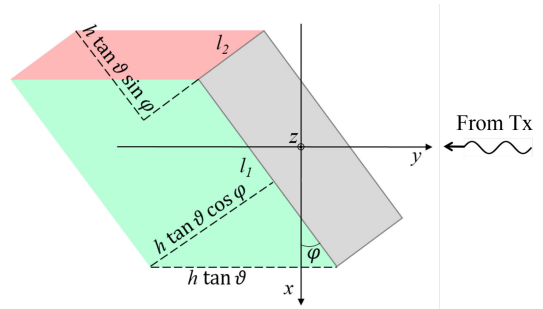


Fig. 6. Shadowing effects caused by the ship. The green and red parallelograms denote portions of the sea surface not illuminated by the impinging wave due to the presence of the ship (gray rectangle) and, therefore, they no longer contribute to the signal scattered off the sea.

accounts for all those rays scattered from the sea surface after a reflection from the ship hull; similarly, the sea-hull term includes the rays reflected from the ship hull after being scattered from the sea surface. Double-bounce terms coincide in amplitude and phase in the backscattering direction—which requires the transmitter, the receiver and the target being aligned—regardless of the sea state and the ship orientation. Conversely, they are no longer the same in a generic bistatic configuration as the ray's paths and local incidence angles on both the ship hull and the sea surface are different in the two contributions. Finally, a further reflection of the hull-sea term on the ship hull leads to the triple-bounce hull-sea-hull scattering, which, hence, comprises two reflections over the ship hull and a single reflection on the sea surface (see blue lines in Fig. 5). It is noteworthy that the sea-hull-sea counterpart does not exist for the considered target geometry, as the vertical hull always make the ray coming from below be reflected upwards. In addition, as opposed to the single-bounce term, multiple-bounce contributions depend, among other parameters, on the ship orientation, the relative position of the transmitter, receiver and ship, and the sea state, i.e., wind speed.

It is worth noting that, at variance of the deterministic single-bounce scattering term, multiple-bounce contributions are random, and, therefore, only their statistics can be analytically derived, typically mean and mean square value. Under GO, the evaluation of the mean square value requires the scattering area be much larger than the correlation length of the rough surface. Such an assumption can be reasonably assumed valid, here, as the sea surface region contributing to the ship RCS (see green and red areas in Fig. 6) is much larger than typical sea surface roughness correlation length values [27].

Once the different scattering contributions have been evaluated, the ship RCS is computed as follows:

$$\sigma_t = 4\pi r^2 \frac{\langle |\underline{E}_s|^2 \rangle}{|\underline{E}_i|^2} \quad (1)$$

where r is the range coordinate of the observation point, $\langle |\underline{E}_s|^2 \rangle$ stands for the mean square value of the overall EM field scattered by the ship, \underline{E}_i is the incident field. It is worth mentioning that the scattering problem in [21] assumes a deterministic ship target model, whereas the surrounding sea surface is described in a stochastic framework. Therefore, the multiple-bounce scattering

contributions are stochastic 3-D processes themselves and cause the overall field scattered by the ship \underline{E}_s to be a random variable in any point, as well. Due to the expectation operator, the ship RCS results in a deterministic function of various parameters, including system parameters (operating frequency, transmitter elevation angle, receiver elevation, and azimuth angles), ship parameters (dimensions, orientation, material composition), and scene parameters (wind speed, sea temperature, and salinity).

Interestingly, the RCS defined according to (1) does not consider the ship target disentangled from its surrounding environment, but accounts for the coupling effects between the ship and the sea surface, which justifies its dependence upon sea parameters. Such an approach can be found in some works, e.g., [25], [28]–[30].

Finally, it is worth mentioning that, despite the simplicity of the target geometry, the monostatic RCS model in [25] has been successfully adopted for ship detection applications using SAR imagery [31], [32].

III. SIMULATION OF GNSS-R DELAY-DOPPLER MAPS

In this Section, we describe the algorithm for the simulation of GNSS-R DDMs of the ocean environment in the presence of ships. The proposed simulation tool is based on the simulator originally proposed in [33], which is capable of simulating the GNSS-R DDM of an ocean surface. We have properly modified that simulator to include the possible presence of a ship, whose scattering is described by the model introduced in [21] and summarized in Section II. Among the different simulation algorithms available in the literature, we selected the one in [33] for its reliability and efficiency. In fact, the approach proposed in [33] is based on a stochastic modeling of the signal reflected off the sea surface and, therefore, both the deterministic (mean square value) and the random (speckle) components of the scattered signal are accounted for in an efficient way. In addition, thanks to the stochastic modeling, the generation of sea surface roughness maps is not required—as, for instance, the facet-based approach in [34]—which leads to excessive computational complexity in a spaceborne scenario due to the scene extent large compared to the GNSS wavelength. Moreover, the algorithm in [33] properly evaluates the autocorrelation function (ACF) of the GPS pseudorandom noise sequences by accounting for the plateau outside the main ACF lobe. This last feature is of key relevance in detection applications, as it allows for properly discriminating weak target responses from secondary peaks of the ACF. Last but not least, the approach in [33] is derived under the same assumptions on both the EM scattering model and the sea surface as the analytical ship RCS model in [21]. In particular, both works describe the sea surface as a normally-distributed stochastic process and derive the scattered signal under KA-GO.

By using the formalism employed in [33], the signal $U_m(t)$ scattered by the m -th delay-Doppler cell is, here, expressed as

$$U_m(t) = \mathcal{D}_m \frac{e^{-ik(R_m+R_{0m})}}{2R_m R_{0m}} a(t - \tau_m) e^{-2\pi i f_{D_m} t} F_m \quad (2)$$

TABLE I
LIST OF SYMBOLS FOR THE j -TH DELAY-DOPPLER CELL

Symbol	Definition
$U_j(t)$	Overall signal received
$U_{j,s}(t)$	Signal scattered from the sea surface
$U_{j,t}(t)$	Signal scattered from the ship
\mathcal{D}_j	Antenna pattern
\mathcal{R}_j	Reflection coefficient
k	EM wavenumber
R_j	Distance from surface point to receiver
R_{0j}	Distance from surface point to transmitter
$a(t)$	Transmitted waveform
τ_j	Delay lag
f_{D_j}	Doppler shift
σ_t	Ship RCS
θ_t	Extra-phase term

where the factor F_m accounts for the scattering properties of the illuminated surface and it will differ according to whether the cell includes or does not include a ship. All the other symbols appearing in (2) are defined in Table I.

If the delay-Doppler cell only contains the sea surface, we can rely on [33], and the signal $U_{m,s}(t)$ scattered by the portion of the sea surface enclosed in the m -th delay-Doppler cell is modeled as a 2-D random walk, i.e., as the sum of a random number $N_m(t)$ of contributions from elementary scatterers within the cell. According to the stationary-phase points approximation, such scatterers are identified with those surface points fulfilling the specular reflection condition. Therefore, [33]

$$U_{m,s}(t) = \mathcal{D}_m \frac{e^{-ik(R_m+R_{0m})}}{2R_m R_{0m}} a(t - \tau_m) e^{-2\pi i f_{D_m} t} \mathcal{R}_m \times \sum_{k=1}^{N_m(t)} A_k(t) e^{i\psi_k(t)} \quad (3)$$

where $A_k(t)$ and $\psi_k(t)$ stand for the amplitude and phase of the scattering contribution from the k th specular point, respectively. For large expected value of $N_m(t)$, the random walk model tends to a compound-Gaussian process and the scattered signal $U_{m,s}(t)$ can be recast as [33]

$$U_{m,s}(t) = \mathcal{D}_m \frac{e^{-ik(R_m+R_{0m})}}{2R_m R_{0m}} a(t - \tau_m) e^{-2\pi i f_{D_m} t} \times \mathcal{R}_m \sqrt{S_m} G_m \quad (4)$$

assuming that the decorrelation time of the compound-Gaussian process is much larger than the code chip length. By comparing (2) and (4), it is easily recognized that $F_m = \mathcal{R}_m \sqrt{S_m} G_m$ and that this term brings information about the scattering features of the sensed sea surface. Indeed, its mean square value represents the RCS of the portion of sea surface enclosed in the delay-Doppler cell. In addition, S_m is the modulating component accounting for the number of specular points within the cell and follows a Gamma distribution [33]; G_m is the normally-distributed component accounting for random phase fluctuations of the elementary scatterers, and, therefore, it is also referred to as the speckle component [33]. Its variance σ_m^2 is demonstrated to be proportional to the area \mathcal{A}_m of the delay-Doppler cell

considered [33], i.e.,

$$\sigma_m^2 = K_{\zeta_x \zeta_y} \mathcal{A}_m \quad (5)$$

where $K_{\zeta_x \zeta_y}$ depends on the local slopes distribution.

Let us now assume that the j -th delay-Doppler cell also includes a ship target of dimensions (length \times width \times height) $l_1 \times l_2 \times h$. The overall signal scattered from that cell can be expressed as

$$U_j(t) = U_{j,s}(t) + U_{j,t}(t) \quad (6)$$

where $U_{j,s}(t)$ is the contribution from the sea surface and $U_{j,t}(t)$ is the overall signal scattered from the ship and including its interactions with the surrounding sea. It is, here, modeled as

$$U_{j,t}(t) = \mathcal{D}_j \frac{e^{-ik(R_j + R_{0j})}}{2R_j R_{0j}} a(t - \tau_j) e^{-2\pi i f_{D_j} t} \sqrt{\sigma_t} e^{i\theta_t}. \quad (7)$$

In particular, the term F_j in (2) is, here, assumed a complex factor whose amplitude is the square root of the ship RCS σ_t , computed according to the model of [21] as illustrated in Section II, whereas θ_t accounts for an additional path term, which is, here, modeled as $\theta_t \sim U(0, 2\pi)$. It is worth mentioning that, according to the RCS definition in (1), the amplitude of the signal reflected off the ship is assumed proportional to the square root RCS defined as in (1), i.e., fluctuations of the target RCS are neglected, whereas the uncertainty in the signal path length are accounted for in the random extra phase term.

It is also worth noting that (7) is consistent with a diffuse scattering model, which is a reasonable assumption as discussed in Section II.

In presence of the ship target, the signal scattered from the sea $U_{j,s}(t)$ can still be expressed through (3) and (4), as long as the area of the scattering sea surface is properly evaluated by accounting for the presence of the ship. Accordingly, the area term in (5) has to be formally substituted with a new area term $\mathcal{A}_{j,st}$, which is computed as

$$\mathcal{A}_{j,st} = \mathcal{A}_j - \mathcal{A}_{\text{target}} - \mathcal{A}_{\text{shadow}} \quad (8)$$

where \mathcal{A}_j is the total area of the j -th delay-Doppler cell, $\mathcal{A}_{\text{target}}$ is the area of the horizontal ship faces, i.e., $\mathcal{A}_{\text{target}} = l_1 l_2$, whereas $\mathcal{A}_{\text{shadow}}$ is the portion of the sea surface shadowed by the ship. The latter, then, accounts for the shadowing effects caused by the ship target and is evaluated as (see Fig. 6)

$$\mathcal{A}_{\text{shadow}} = l_1 h \tan \vartheta |\cos \varphi| + l_2 h \tan \vartheta \sin \varphi \quad (9)$$

where $\vartheta \in [0, \pi/2]$ is the transmitter look angle and $\varphi \in [0, \pi]$ is the orientation angle of the ship, defined as the angle between the l_1 edge of the ship, and the positive x -semiaxis.

Finally, it is worth mentioning that, in the evaluation of the signal scattered from the sea $U_{j,s}(t)$, the compound-Gaussian model used in [33] and expressed in (4) still holds as long as the ship size is much smaller than the resolution cell, which is a reasonable assumption in GNSS-R.

IV. SIMULATION RESULTS

In this section, we carry out a feasibility analysis of GNSS-R for ship detection applications by using the algorithm presented

TABLE II
LIST OF PARAMETER VALUES FIXED THROUGHOUT
THE WHOLE SIMULATION STUDY

Symbol	Definition	Value
$[l_1, l_2, h]$	Ship size	[360 m, 60 m, 70 m]
f_0	GNSS signal frequency	1571 MHz
pol	Receiving polarization channel	RHCP or LHCP
T_{sea}	Seawater temperature	20°C
S_{sea}	Seawater salinity	35 ppm
S_p	Sea spectrum	Pierson-Moskowitz
F	Receiver noise figure	3.6 dB (spaceborne) 1.92 dB (airborne)
B_W	Receiver bandwidth	2.5 MHz (spaceborne) 24 MHz (airborne)
G_r	Receiver antenna gain	13.3 dBi (spaceborne) 15.05 dBi (airborne)
B_r	3dB receiver antenna beamwidth	29 deg. (spaceborne) 36 deg. (airborne)

in the previous sections. Both spaceborne and airborne configurations are considered and simulated in the following. The simulation study is two-fold. First, we assess ship detection through DDMs in selected scenarios that represent the optimal conditions for target visibility. Indeed, the link budget in [19] and [20] predicts low SNR values for the echo reflected by the ship target at different operating conditions and scene configurations. Therefore, it is useful to assess ship visibility under optimal detection conditions. This first part of the simulation analysis is addressed in Section IV-A. Then, in Section IV-B, we analyze the target detectability as a function of the target location within the observed scene. A key aspect of our feasibility study is the simulation of thermal noise, which represents the most relevant disturbance in GNSS-R observables for target detection applications [19]. Another relevant aspect is related to the receiver antenna pattern that can vary significantly over the DDM, thus impacting over the measured target SNR. With regards to both aspects, we refer to the SGR-ReSi [35] and to the GOLD-RTR [36] instruments and front ends for spaceborne and airborne configurations, respectively. Accordingly, two slightly different versions of the simulator proposed in Section III have been adopted for simulation purposes accounting for the different antenna patterns, noise figures, and signal losses.

For the evaluation of the scattering from the ship and the sea surface, the parameters listed in Table II are set once and for all throughout the whole simulation study. It is worth noting that the ship size is set according to the dimensions of the *Symphony of the Seas*, the world's largest passenger ship by gross tonnage currently in operation, owned by Royal Caribbean International.

In addition, ship detection capabilities are assessed by evaluating the SNR of the target response. For a better insight about the target detectability using incoherently-averaged DDMs, which represent the current main product of GNSS-R missions, the SNR is calculated after the incoherent integration step. In particular, it is evaluated as the ratio between the peak of the DDM of only the ship, i.e., without sea clutter and thermal noise, and the standard deviation of the DDM of only thermal noise, i.e., without sea clutter and target. Indeed, the mean value of the latter DDM, recognized as the thermal noise mean square value, does not affect the SNR as it can be estimated and suppressed in measured data.

The thermal noise power P_N at the output of the receiver RF front end is evaluated as follows:

$$P_N = k_B(T_a + T_e)B_W \quad (10)$$

where k_B is the Boltzmann constant; T_a is the receiving antenna noise temperature, which is set equal to $T_a = 99.4$ K [37]; T_e is the receiver noise temperature, which is evaluated as $T_e = T_0(F - 1)$ with $T_0 = 290$ K. The parameters B_W and F are defined in Table II for both the spaceborne and the airborne configurations.

Finally, it is worth mentioning that 1) the whole simulation study is, here, limited to GPS C/A navigation signaling only; 2) standard 1 ms coherent and 1 s incoherent integration times are adopted throughout the whole simulation study. This latter point deserves a comment. Indeed, despite playing an important role for target detection purposes, we will not analyze the role of the integration times and, therefore, adopted the typical values used in current GNSS-R missions for the following reasons.

First, in designing a GNSS-R receiver specifically conceived for maritime surveillance, there are, at least in principle, numerous degrees of freedom that can be exploited to maximize the detection performance. Due to the large number of parameters influencing the SNR, it would be preferable to conceptually classify them in few (with uncorrelated effects on the SNR) categories. In our case, two categories can be defined: 1) parameters related to the GNSS-R system—acquisition geometry, polarization, receiver height—which are analyzed in this work and 2) processing parameters, e.g., the coherent and incoherent integration times or, definitely, the signal processing chain, which is likely to play a key role in ship detectability but whose analysis goes outside the scope of this work.

Second, a change in the coherent integration time would require an accurate analysis of the coherence time of the ship return, which, again goes outside the scope of this work. If it is true that a non-negligible quota of the received power is due to the coupling effects with the sea surface, the coherence time is expected to depend on the sea state as well and it is reasonable to expect that it would not differ that much from the coherence time of sea.

Finally, it is worth mentioning that the coherence time of the ship is expected to depend even on the acquisition geometry due to the different scattering mechanisms arising in the different observation angles: this justifies the conceptual research path of analyzing first the system parameters, then the processing one. Accordingly, analyzing the role of the GNSS signaling scheme and the GNSS-R processing chain, despite being an interesting topic, goes outside the scope of this work.

A. Optimal Detection Scenarios Under GO Approximation

Here, we are interested in analyzing ship visibility in both spaceborne and airborne GNSS-R DDMs under favorable detection conditions. Such conditions are defined by the set of parameter values that maximize the target RCS in a specific N -dimensional subspace. In particular, the maximum of the ship RCS is found in terms of the acquisition geometry angles, ϑ , ϑ_s , φ_s , the ship orientation φ and the local wind speed

TABLE III
LIST OF PARAMETER VALUES FOR THE FAVORABLE DETECTION SCENARIOS

Parameter	Scenario A	Scenario B	Scenario C	Scenario D
h_R	600 km	600 km	10 km	10 km
pol	LHCP	RHCP	LHCP	RHCP
ϑ	15°	15°	15°	15°
ϑ_s	15°	15°	15°	15°
φ_s	90°	90°	90°	90°
φ	0°	0°	0°	0°
U_{10}	20 m/s	5 m/s	20 m/s	5 m/s
RCS [dBsm]	31.86	49.47	31.86	49.47
f_D [Hz]	137.25	137.25	2.77	2.77
τ [C/A chip]	227.80	227.80	4.71	4.71

U_{10} . The lower and upper bounds of the transmitter and the receiver look angles and wind speed are set according to the limits of validity of the GO model [21], [38]. In particular, $\vartheta \in [2^\circ, 15^\circ]$, $\vartheta_s \in [2^\circ, 15^\circ]$, $U_{10} \in [5, 20]$ m/s have been considered. Conversely, no restrictions are applied to the receiver azimuth angle φ_s in order to consider both the conventional forward-scattering geometry and the nonstandard backward one discussed in [10], [19], and [20]. Indeed, according to the scattering reference frame in Fig. 4, the specular reflection point is defined by $\vartheta_s = \vartheta$ and $\varphi_s = 270^\circ$, whereas the backscattering point has $\vartheta_s = \vartheta$ and $\varphi_s = 90^\circ$.

Additionally, recalling that, according to [21], the transmitter lays in the ($y > 0, z > 0$) space, here we define a forward-scattering acquisition geometry if the receiver lays in the ($y < 0, z > 0$) space, i.e., $\varphi_s \in [180^\circ, 360^\circ]$, whereas the backscattering configuration is defined by a receiver in the ($y > 0, z > 0$) space, i.e., by $\varphi_s \in [0^\circ, 180^\circ]$.

The range of the aspect angle φ is limited to $[0^\circ, 90^\circ]$ due to the target symmetry, without loss of generality. Finally, step sizes of 1° and 1 m/s have been considered for the four angles and wind speed, respectively. Remaining parameters for the evaluation of the ship RCS—ship size, operating frequency, polarization, seawater temperature and salinity, and sea spectrum—are set according to Table II. It is noteworthy that the delay-Doppler region analyzed by the GNSS-R processor is an artificial boundary that can be arbitrarily set by the system designer according to the applications requirements. Therefore, no restrictions are, here, applied on the delay and Doppler coordinates of the target positions in the scenarios analyzed.

The favorable detection conditions have been evaluated in four scenarios defined by combining receiver altitude (spaceborne and airborne) and receiving polarization channel (LHCP and RHCP). In the selected scenarios, the receiver is located at an altitude of 600 and 10 km for the spaceborne and the airborne configurations, respectively.

The complete list of optimization parameters for the selected scenarios is presented in Table III, while the relative geometry between the transmitter, the receiver and the target is shown in Fig. 7 for the four scenarios analyzed.

The optimization outcomes deserve some comments.

First, the target RCS depends on the receiving polarization channel but not on the receiver altitude and, hence, the same optimal parameter and ship RCS values are obtained at spaceborne and airborne altitudes for each polarization.

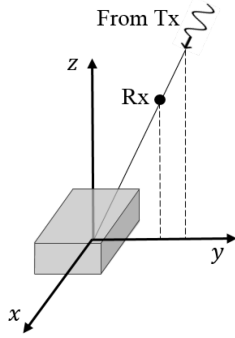


Fig. 7. Relative geometry for the favorable detection conditions, scenarios A–D. Parameter values are listed in Tables II and III.

Second, in all the scenarios considered, best detection conditions, i.e., largest RCS values are measured in the backscattering direction, as witnessed by the achieved values of ϑ , ϑ_s , and φ_s . Indeed, from [21] it emerged that, under GO approximation, the ship behaves like a mirror surface, thus reflecting the impinging energy in a direction, which depends on the target orientation and with an angular spreading, which increases with the local wind speed.

Third, switching from the conventional LHCP polarization channel to the nonstandard RHCP one allows for a significant increase of the ship RCS (see Table III). It is also worth noting that opposite sea state conditions are favorable for detecting ship targets in different polarization channels. Actually, in a backscattering configuration, the LHCP component of the ship response is dominated by the triple-scattering term, which increases with increasing wind speed as it depends on the EM energy backscattered off the sea surface (see dark blue lines in Fig. 5). Conversely, the more favorable RHCP channel is dominated by the double-bounce scattering contributions, which are stronger at lower wind speed as they depend on the sea specular response (see red lines in Fig. 5).

Moreover, due to the much slower variation of the receiver viewing angle ϑ_s at higher altitudes, best detection conditions from spaceborne data are obtained at delay lags much larger than typical ranges processed for remote sensing applications (see parameters for Scenarios A and B in Table III). This requires a proper design of the GNSS-R processing and data selection/storing schemes.

Finally, the optimization problem has been undertaken neglecting the transmitter and receiver antenna radiation patterns. Indeed, they do not influence the target RCS, even if they may significantly reduce the target echo. However, it is worth mentioning that the considered range of ϑ_s is close or within the 3 dB receiver antenna beamwidth for spaceborne and airborne configurations, respectively (see Table II). Accordingly, the receiving antenna does not significantly impact the target response in all the scenarios analyzed.

Simulation results relevant to the four selected scenarios are presented in Fig. 8, where all DDMs are shown in watt unit. In this simulation setup, the target has ECEF coordinates $(0, 0, r_E)$, where r_E is the local equivalent earth radius and the specular reflection point has delay-Doppler coordinates $(0, 0)$. However,

for spaceborne scenarios the processed delay-Doppler region has been centered on the backscattering point—which corresponds also to the target positions—rather than the specular reflection point. As a result, the typical horseshoe shape is not visible in the corresponding DDMs of sea clutter.

When considering a standard spaceborne LHCP GNSS-R [see Fig. 8(a)], the signal scattered from the target—that exhibits the typical WAF shape [see Fig. 8(b)]—is several orders of magnitude below the thermal noise power (SNR around -46 dB), which in turn is below the sea clutter after the incoherent integration. Accordingly, in such a configuration, the sea clutter dominates, as witnessed by the DDM values in Fig. 8(a)–(c).

Let us move to the RHCP case, see Fig. 8(e)–(h) relevant to Scenario B. In this case, the target RCS is increased by 17.61 dB with respect to the previous case (see Table III). This is due to the double-bounce scattering contributions, which are predominantly the same polarization as the transmitted waveform, i.e., RHCP. The much larger RCS results in a much stronger return from the ship target, as shown in Fig. 8(f). Despite such a significant increase, the ship return is still well below the thermal noise level, achieving a peak value of around 3.11×10^{-22} W, i.e., an SNR of about -29 dB. At the same time, the sea clutter is significantly attenuated, being of the same order of magnitude as the target response [see Fig. 8(g)]. As a result, the overall DDM is largely dominated by thermal noise [see Fig. 8(e)–(g)] and ship detection is still unfeasible even under optimal detection conditions.

Simulation results relevant to the airborne scenarios are shown in Fig. 8(i)–(l) and (m)–(p) for the LHCP and RHCP cases, respectively. The increased target signal power provided by the lower receiver altitude is still well below the thermal noise in the standard LHCP configuration [see Fig. 8(j)]. Indeed, under optimal detection conditions, the signal scattered from the ship achieves a peak power of about 3.569×10^{-20} W, which corresponds to an SNR of about -10.45 dB. Conversely, the stronger sea clutter largely dominates the thermal noise such that the overall noisy DDM and the noise-free DDM of only sea clutter look very similar, compare Fig. 8(i) and (k).

Finally, when switching to the RHCP channel, the target emerges above the noise level, as shown in Fig. 8(m). Thanks to the more favorable polarization channel, the target peak power is around 2.058×10^{-18} W, which corresponds to an SNR of about 7.16 dB. Conversely, the RHCP component of sea clutter is strongly attenuated with respect to the LHCP one as the peak signal level is around 4.59×10^{-20} W, thus making unnecessary any clutter suppression step, as instead required in standard GNSS-R [9]. Accordingly, a simple hard-thresholding detector can finally reveal the target.

B. Role of the Target Position

In this second part of the simulation study, we address the variation of the detection performance within the DDM for different spaceborne and airborne altitudes. To this end, we build an SNR map obtained by changing the ship position through several runs, whereas the transmitter and the receiver positions are kept constant in any configuration analyzed.

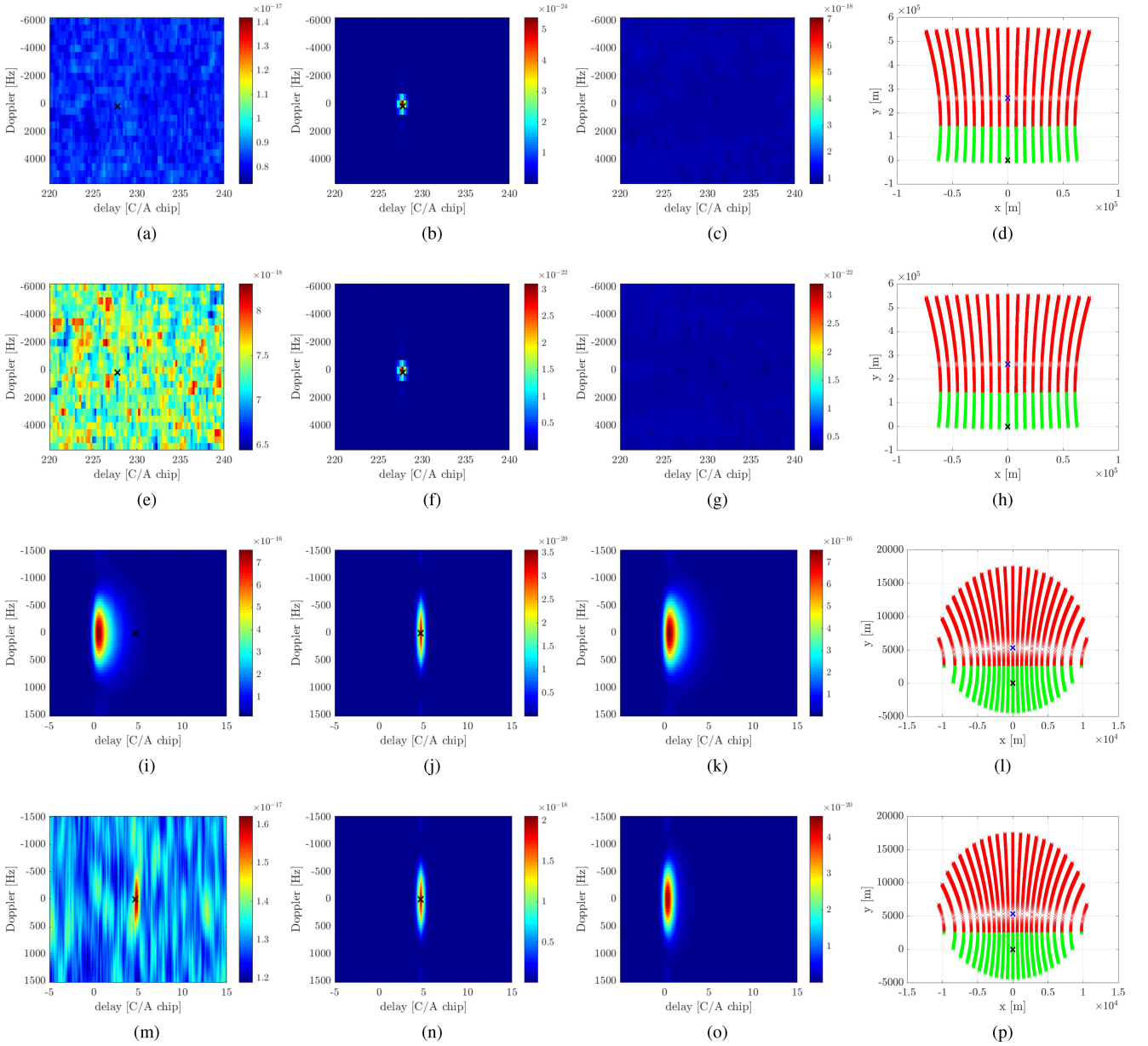


Fig. 8. Simulated DDMs for (a)–(d) Scenario A (spaceborne - LHCP), (e)–(h) Scenario B (spaceborne - RHCP), (i)–(l) Scenario C (airborne - LHCP) and (m)–(p) Scenario D (airborne - RHCP) comprising (a), (e), (i), (m) sea clutter, target and thermal noise. (b), (f), (j), (n) only target. (c), (g), (k), (o) only sea clutter. (d), (h), (l), (p) Scattering area in Earth-Centered Earth-Fixed (ECEF) coordinates with green and red points identifying the backscattering and the forward-scattering regions, respectively. In this simulation setup, the ship target has ECEF coordinates $(0, 0, r_E)$, r_E being the local equivalent Earth radius. The specular reflection point and the target, which is located at the backscattering point, are highlighted as a blue and black cross, respectively. Simulation parameters are listed in Tables II and III.

From the simulation analysis carried out in Section IV-A, it emerged that a GNSS-R instrument receiving the LHCP component of the scattered signal, would be hardly exploited for detecting ship targets even at airborne altitudes. Therefore, here, we investigate the role of the target position in the RHCP polarization channel only.

Simulation parameters are set as follows: the transmitter look angle ϑ is set to 4° and 15° in spaceborne and airborne simulations, respectively; wind speed is set to 5 m/s, whereas ship orientation is $\varphi = 0^\circ$. Remaining parameters are set according to Table II. In all configurations, the SNR map has been obtained

with about 1000 target positions uniformly spaced over the whole allowed region—i.e., the subset of the considered delay-Doppler coordinates, which correspond to physical areas over the earth’s surface—and covering only one of the two ambiguity regions. For any fixed target position, the simulation is run and the SNR is evaluated as detailed in Section IV and its value is stored in the SNR map at the same delay-Doppler coordinates of the target. By repeating the abovementioned procedure for all the target positions, the SNR map is finally obtained.

Simulation results are presented in Figs. 9 and 10 for the spaceborne (600, 400, 200, 100 km altitude) and airborne

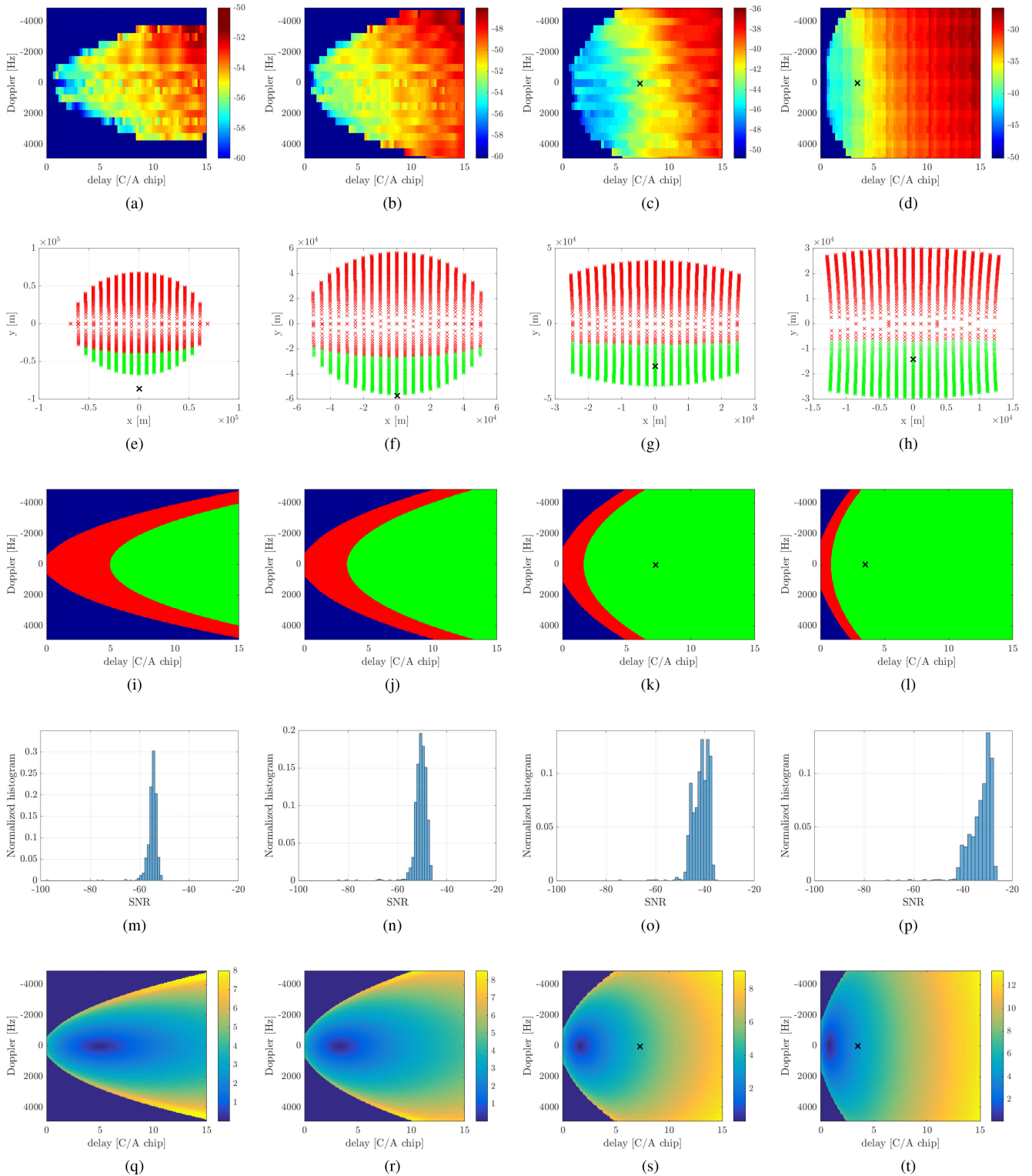


Fig. 9. Spaceborne RHCP GNSS-R receiver at an altitude of (a), (e), (i), (m), (q) 600 km, (b), (f), (j), (n), (r) 400 km, (c), (g), (k), (o), (s) 200 km, (d), (h), (l), (p), (t) 100 km. (a)–(d) SNR map in dB. (e)–(h) Scattering area in ECEF coordinates with green and red points identifying the backscattering and the forward-scattering regions, respectively. The ambiguity-free line is approximately at $y = 0$. The receiver is moving parallel to the x -axis. (i)–(l) Backscattering (green) and forward-scattering (red) points for the ambiguity region $y \leq 0$. (m)–(p) Normalized histogram of the SNR maps. (q)–(t) DDM of ϑ_s in degrees. In this simulation setup, the specular reflection point has ECEF coordinates $(0, 0, r_E)$. The backscattering point is highlighted as a black cross.

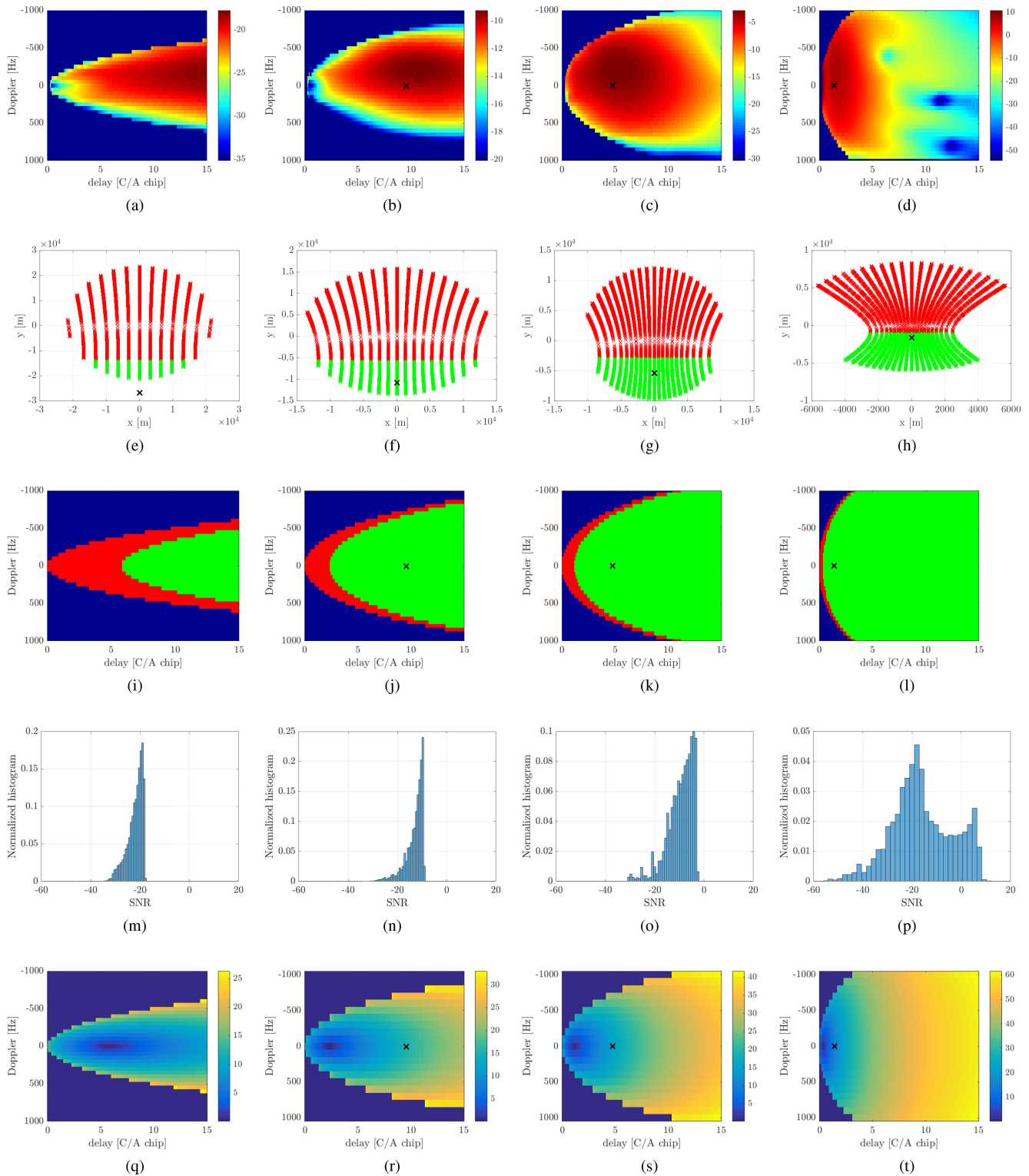


Fig. 10. Airborne RHCP GNSS-R receiver at an altitude of (a), (e), (i), (m), (q) 50 km, (b), (f), (j), (n), (r) 20 km, (c), (g), (k), (o), (s) 10 km, (d), (h), (l), (p), (t) 3 km. (a)–(d) SNR map in dB. (e)–(h) Scattering area in ECEF coordinates with green and red points identifying the backscattering and the forward-scattering regions, respectively. The ambiguity-free line is approximately at $y = 0$. The receiver is moving parallel to the x -axis. (i)–(l) Backscattering (green) and forward-scattering (red) points for the ambiguity region $y \leq 0$. (m)–(p) Normalized histogram of the SNR maps. (q)–(t) DDM of ϑ_s in degrees. In this simulation setup, the specular reflection point has ECEF coordinates $(0, 0, r_E)$. The backscattering point is highlighted as a black cross.

TABLE IV
SYNTHETIC PERFORMANCE PARAMETERS (SNR) IN DECIBEL

Receiver height	Min	Max	Mean	Std. dev.
600 km	-97.79	-51.36	-54.93	2.60
400 km	-84.15	-46.03	-50.65	2.89
200 km	-73.84	-35.87	-41.70	3.39
100 km	-70.18	-26.57	-32.85	4.62
50 km	-36.21	-12.74	-22.08	4.29
20 km	-45.81	-9.24	-13.07	4.43
10 km	-30.37	-2.78	-9.56	5.34
3 km	-54.46	10.73	-15.92	12.49

(50, 20, 10, 3 km altitude) configurations, respectively. SNR maps are shown in Figs. 9(a)–(d) and 10(a)–(d), whereas Figs. 9(e)–(h) and 10(e)–(h) show the scattering area in ECEF coordinates with green and red points marking the backscattering and the forward-scattering regions, respectively. In this simulation setup, the specular reflection point has ECEF and delay-Doppler coordinates $(0, 0, r_E)$ and $(0, 0)$, respectively. The black cross corresponds to the backscattering point, if present within the processed delay-Doppler domain. All the targets have been located in the ambiguity region defined by $y \leq 0$, being the ambiguity-free line approximately located at $y = 0$. Figs. 9(i)–(l) and 10(i)–(l) show the backscattering/forward-scattering distribution of the selected ambiguity region $y \leq 0$ (green and red areas, respectively). For a quantitative analysis, the normalized histogram of the SNR maps is shown in Figs. 9(m)–(p) and 10(m)–(p), whereas synthetic SNR statistics in dB are listed in Table IV.

For a 600-km-altitude receiver, the SNR map exhibits lower values than that achieved in the corresponding optimal conditions (Scenario B in Section IV-A) ranging from around -98 dB to -51 dB [see Fig. 9(a)]. Similarly, the largest SNR value at 10 km altitude is -2.78 dB, lower than 7.16 dB measured under optimal conditions. It is worth noting that the SNR assumes larger values in the backscattering region as opposed to in the forward-scattering one, regardless of the receiver altitude. This is more clearly visible at altitudes not larger than 20 km, where the best detection conditions are achieved close to the backscattering point (see Fig. 10(b)–(d)). However, poor detection performances are expected from the satellite configurations considered, as the largest SNR is around -26 dB at 100 km altitude. Conversely, interesting results are obtained at altitudes not larger than 20 km, where SNR values greater than 10 dB are achieved at 3 km altitude. It is worth noting that the maximum values of the SNR maps achieved here and reported in Table IV represent the largest values over the allowed region achieved in the considered scenarios, whose parameters are listed at the beginning of this Section IV-B. As opposed to the simulation study in Section IV-A, the scenarios analyzed here do not represent the best possible configurations in terms of geometry, ship orientation, and wind speed, as also witnessed by the fact that the maximum SNR achieved at 10 km (-2.78 dB) is below the SNR value achieved in Scenario D at the same altitude (7.16 dB) (see Section IV-A).

Interestingly, at lower altitudes it is experienced a larger variation of SNR, whose standard deviation ranges from 2.60 dB at 600 km to 12.49 dB at 3 km, see also the normalized histograms

in Figs. 9(m)–(p) and in 10(m)–(p). This is due to the higher dynamics of the receiver look angle ϑ_s over the delay-Doppler domain at lower altitudes [see Figs. 9(q)–(t) and 10(q)–(t)]. Hence, such larger variations make both ship RCS values and receiver antenna pattern significantly vary over the scattering area. Finally, it is worth noting that the lower is the receiver altitude, 1) the closer are the backscattering and the specular reflection points; 2) the smaller the detectable ship.

V. CONCLUSION

This article has presented a feasibility study of the ship detection problem using GNSS-R DDMs via simulation tools. As simulators available in the literature can only deal with bare soil and sea surfaces, here we described a new DDM simulation algorithm able to account for the presence of ship targets over the scattering sea surface. The proposed approach for the generation of DDMs relies on a previous stochastic simulator for bare sea surfaces and introduces a proper modification of the received signal model in order to account for the ship target, which is, here, modeled as a parallelepiped with smooth faces. For this target model, a closed-form analytical scattering model has been recently developed and adopted, here, for the evaluation of the ship RCS. An important feature of the adopted RCS model is the modeling of the multiple-bounce scattering mechanisms between the ship hull and the surrounding sea surface. Scattering from both sea surface and ship is described in the framework of the GO approximation.

The developed algorithm has then been used to assess ship detectability in both spaceborne and airborne GNSS-R DDMs and analyze what are the preferable conditions for ship detection using the typical GNSS-R signal processing chain. First, ship visibility was addressed in both LHCP and RHCP receiving polarization channels in optimal detection conditions under GO validity limits. To this end, the ship RCS was maximized in terms of scattering angles, ship orientation, and sea state. The simulation analysis confirmed the benefits of the RHCP channel with respect to the conventional LHCP one, as already found in previous link budget analyzes. In addition, all optimal conditions were achieved in the more favorable backscattering geometry. It was even found that ship detection is hardly manageable with spaceborne GNSS-R, as the achieved SNR is well under 0 dB.

The second part of the simulation study was aimed at evaluating detection performance variation over the delay-Doppler domain. Here, we focused on the RHCP channel only, as it is preferable for detection purposes, and analyzed different receivers altitudes. The largest SNR values were obtained in the backscattering region due to the double-bounce scattering featuring the signal reflected from the ship target. Moreover, SNR values larger than 0 dB were achieved at airborne altitudes, where better performance was found close to the backscattering point for a ship facing the transmitting GNSS station.

To summarize the above mentioned outcomes, it can be stated that ship detection is hardly manageable using satellite data, whereas interesting results were achieved at airborne altitudes provided that the aircraft is approximately between the GNSS satellite and the target, and that appropriate RHCP polarization is probed.

Notwithstanding, there is still much room for further investigations in the field. Indeed, the system design guidelines provided in this work should be complemented by the development of a dedicated signal processing chain whose investigation is a matter of future work. Actually, the simulation study assessed the optimal detection conditions assuming typical GNSS-R processing, which collects the signal scattered from a region surrounding the specular reflection point. In this context, satellite GNSS-R data exhibited poor applicability in target detection applications due to the low signal level compared to the thermal noise power using both standard and nonstandard configurations. However, the signal processing chain is expected to play a key role in target detection performance. Indeed, longer integration times, SAR-like processing and exploitation of DDMs time sequence might be beneficial to a stronger reduction of the thermal noise. In this direction, track-before-detect techniques might be explored to account for the relative movements between the target, the transmitter and the receiver. Accordingly, further investigations are required for the design of a processing chain suited to the detection problem, i.e., by analyzing the region around the backscattering point, where larger SNR values were achieved, or better tuning the integration times (coherent and incoherent) to improve target visibility.

From a technological viewpoint, the adoption of digital beamforming techniques or multibeam antennas may be useful to further enhance the signal scattered from the ship target in the backscattering region at a cost of a more complex receiver front end.

In addition, due to the limited applicability of the GO backscattering model, we focused our analysis to low incidence angles, i.e., large elevation angles of GNSS stations. However, larger ship RCS values in the backscattering configuration might be obtained at larger incidence angles, which would be addressed by analyzing larger delay-Doppler coordinates or by processing the scattering region around the backscattering point. Therefore, an important research activity would rely on the development of further scattering models for both the sea surface and the ship target for the deployment of GNSS-R simulation tools suited to the backscattering at larger incidence angles.

Finally, only GPS C/A signals have been analyzed in this simulation study. Therefore, it would be interesting to assess ship detectability with other GNSS signals, i.e., GLONASS, Galileo, BeiDou-2, in order to address the GNSS signaling scheme most suited to detection applications. In this direction, the integration of multiple GNSS signals is expected to further improve detection performance and, therefore, represents an interesting research path.

ACKNOWLEDGMENT

The authors would like to thank Surrey Satellite Technology Ltd. for making GNSS-R data collected by TDS-1 available free of charge.

REFERENCES

- [1] M. P. Clarizia and C. S. Ruf, "Wind speed retrieval algorithm for the cyclone global navigation satellite system (CYGNSS) mission," *IEEE Trans. Geosci. Remote Sens.*, vol. 54, no. 8, pp. 4419–4432, Aug. 2016.
- [2] A. Rius, E. Cardellach, and M. Martin-Neira, "Altimetric analysis of the sea-surface GPS-reflected signals," *IEEE Trans. Geosci. Remote Sens.*, vol. 48, no. 4, pp. 2119–2127, Apr. 2010.
- [3] J. F. Marchan-Hernandez *et al.*, "Sea-state determination using GNSS-R data," *IEEE Geosci. Remote Sens. Lett.*, vol. 7, no. 4, pp. 621–625, Oct. 2010.
- [4] M. P. Clarizia, C. S. Ruf, P. Jales, and C. Gommenginger, "Spaceborne GNSS-R minimum variance wind speed estimator," *IEEE Trans. Geosci. Remote Sens.*, vol. 52, no. 11, pp. 6829–6843, Nov. 2014.
- [5] D. Pascual, A. Camps, F. Martin, H. Park, A. A. Arroyo, and R. Onrubia, "Precision bounds in GNSS-R ocean altimetry," *IEEE J. Sel. Topics Appl. Earth Observ. Remote Sens.*, vol. 7, no. 5, pp. 1416–1423, May 2014.
- [6] V. U. Zavorotny and A. G. Voronovich, "Scattering of GPS signals from the ocean with wind remote sensing application," *IEEE Trans. Geosci. Remote Sens.*, vol. 38, no. 2, pp. 951–964, Mar. 2000.
- [7] M. Di Bisceglie *et al.*, "Two-scale model for the evaluation of sea-surface scattering in GNSS-R ship-detection applications," in *Proc. IEEE Int. Geosci. Remote Sens. Symp.*, 2018, pp. 3181–3184.
- [8] V. U. Zavorotny, S. Gleason, E. Cardellach, and A. Camps, "Tutorial on remote sensing using GNSS bistatic radar of opportunity," *IEEE Geosci. Remote Sens. Mag.*, vol. 2, no. 4, pp. 8–45, Dec. 2014.
- [9] A. Di Simone, H. Park, D. Riccio, and A. Camps, "Sea target detection using spaceborne GNSS-R delay-Doppler maps: Theory and experimental proof of concept using TDS-1 data," *IEEE J. Sel. Topics Appl. Earth Observ. Remote Sens.*, vol. 10, no. 9, pp. 4237–4255, Sep. 2017.
- [10] M. P. Clarizia, P. Braca, C. S. Ruf, and P. Willett, "Target detection using GPS signals of opportunity," in *Proc. 18th Int. Conf. Inf. Fusion*, Washington, DC, USA, Jul. 6–9, 2015, pp. 1429–1436.
- [11] A. Di Simone, A. Iodice, D. Riccio, A. Camps, and H. Park, "GNSS-R: A useful tool for sea target detection in near real-time," in *Proc. IEEE 3rd Int. Forum Res. Technologies Soc. Industry*, 2017, pp. 1–6.
- [12] G. Carrie, T. Deloues, J. Mametsa, and S. Angelliaume, "Ship detection based on GNSS reflected signals: An experimental plan," in *Proc. Space Reflecto*, 2011.
- [13] Y. Lu, D. Yang, W. Li, J. Ding, and Z. Li, "Study on the new methods of ship object detection based on GNSS reflection," *Mar. Geodesy*, vol. 36, no. 1, pp. 22–30, 2013.
- [14] H. Ma *et al.*, "Maritime moving target indication using passive GNSS-based bistatic radar," *IEEE Trans. Aerosp. Electron. Syst.*, vol. 54, no. 1, pp. 115–130, Feb. 2018.
- [15] H. Ma, M. Antoniou, A. G. Stove, J. Winkel, and M. Cherniakov, "Maritime moving target localization using passive GNSS-based multistatic radar," *IEEE Trans. Geosci. Remote Sens.*, vol. 56, no. 8, pp. 4808–4819, Aug. 2018.
- [16] F. Santi, F. Peralice, and D. Pastina, "Joint detection and localization of vessels at sea with a GNSS-based multistatic radar," *IEEE Trans. Geosci. Remote Sens.*, vol. 57, no. 8, pp. 5894–5913, Aug. 2019.
- [17] A. K. Brown, "Remote sensing using bistatic GPS and a digital beam-steering receiver," in *Proc. IEEE Int. Geosci. Remote Sens. Symp.*, 2005, vol. 1.
- [18] X. He, M. Cherniakov, and T. Zeng, "Signal detectability in SS-BSAR with GNSS non-cooperative transmitter," *IEE-Proc. Radar, Sonar Navigation*, vol. 152, no. 3, pp. 124–132, Jun. 2005.
- [19] A. Di Simone *et al.*, "Spaceborne GNSS-reflectometry for ship-detection applications: Impact of acquisition geometry and polarization," in *Proc. IEEE Int. Geosci. Remote Sens. Symp.*, 2018, pp. 1071–1074.
- [20] A. Di Simone *et al.*, "Maritime surveillance using spaceborne GNSS-reflectometry: The role of the scattering configuration and receiving polarization channel," in *Proc. IEEE 4th Int. Forum Res. Technol. Soc. Industry*, 2018, pp. 1–5.
- [21] A. Di Simone *et al.*, "Analytical models for the electromagnetic scattering from isolated targets in bistatic configuration: Geometrical optics solution," *IEEE Trans. Geosci. Remote Sens.*, vol. 58, no. 2, pp. 861–880, Feb. 2020.
- [22] A. W. Doerry and B. C. Brock, "Radar cross section of triangular trihedral reflector with extended bottom plate," Sandia Nat. Lab., Albuquerque, NM, USA, Tech. Rep. SAND2009-2993, May 2009.
- [23] D. E. Barrick, *Radar Cross Section Handbook*, vol. 2. New York, NY, USA: Plenumpress, 1970.
- [24] S. L. Ullo, G. Giangregorio, M. di Bisceglie, C. Galdi, M. P. Clarizia, and P. Addabbo, "Analysis of GPS signals backscattered from a target on the sea surface," in *Proc. IEEE Int. Geosci. Remote Sens. Symp.*, 2017, pp. 2062–2065.

- [25] G. Franceschetti, A. Iodice, and D. Riccio, "A canonical problem in electromagnetic backscattering from buildings," *IEEE Trans. Geosci. Remote Sens.*, vol. 40, no. 8, pp. 1787–1801, Aug. 2002.
- [26] B. R. Mahafza, *Radar Systems Analysis and Design Using MATLAB*. Boston, MA, USA: Chapman, 2005.
- [27] D. Xie, K.-S. Chen, and J. Zeng, "The frequency selective effect of radar backscattering from multiscale sea surface," *Remote Sens.*, vol. 11, no. 2, p. 160, 2019.
- [28] J. T. Johnson, "A study of the four-path model for scattering from an object above a half space," *Microw. Opt. Technol. Lett.*, vol. 30, no. 2, pp. 130–134, 2001.
- [29] H. Chen, M. Zhang, and H. C. Yin, "Facet-based treatment on microwave bistatic scattering of three-dimensional sea surface with electrically large ship," *Prog. Electromagn. Res.*, vol. 123, pp. 385–405, 2012.
- [30] M. Man, Z. Lei, Y. Xie, and X. Li, "Bistatic RCS prediction of composite scattering from electrically very large ship-sea geometry with a hybrid facet-based KA and shadow-corrected GRECO scheme," *Prog. Electromagn. Res.*, vol. 60, pp. 35–48, 2014.
- [31] P. Iervolino, R. Guida, and P. Whittaker, "A model for the backscattering from a canonical ship in SAR imagery," *IEEE J. Sel. Topics Appl. Earth Observ. Remote Sens.*, vol. 9, no. 3, pp. 1163–1175, Mar. 2016.
- [32] P. Iervolino and R. Guida, "A novel ship detector based on the generalized-likelihood ratio test for SAR imagery," *IEEE J. Sel. Topics Appl. Earth Observ. Remote Sens.*, vol. 10, no. 8, pp. 3616–3630, Aug. 2017.
- [33] G. Giangregorio, M. di Bisceglie, P. Addabbo, T. Beltramonte, S. D'Addio, and C. Galdi, "Stochastic modeling and simulation of delay–Doppler maps in GNSS-R over the ocean," *IEEE Trans. Geosci. Remote Sens.*, vol. 54, no. 4, pp. 2056–2069, Apr. 2016.
- [34] M. P. Clarizia, C. Gommenginger, M. Di Bisceglie, C. Galdi, and M. A. Srokosz, "Simulation of L-band bistatic returns from the ocean surface: A facet approach with application to ocean GNSS reflectometry," *IEEE Trans. Geosci. Remote Sens.*, vol. 50, no. 3, pp. 960–971, Mar. 2012.
- [35] M. Unwin, P. Jales, J. Tye, C. Gommenginger, G. Foti, and J. Rosello, "Spaceborne GNSS-reflectometry on TechDemoSat-1: Early mission operations and exploitation," *IEEE J. Sel. Topics Appl. Earth Observ. Remote Sens.*, vol. 9, no. 10, pp. 4525–4539, Oct. 2016.
- [36] O. Nogués-Correig, E. C. Galí, J. S. Campderrós, and A. Rius, "A GPS-reflections receiver that computes Doppler/delay maps in real time," *IEEE Trans. Geosci. Remote Sens.*, vol. 45, no. 1, pp. 156–174, Jan. 2007.
- [37] M. Morris, D. D. Chen, and C. S. Ruf, "Earth antenna temperature variability for CYGNSS," in *Proc. IEEE Int. Geosci. Remote Sens. Symp.*, 2016, pp. 846–849.
- [38] W. Fuscaldo, A. Di Simone, L. M. Millefiori, A. Iodice, P. Braca, and P. Willett, "A convenient analytical framework for electromagnetic scattering from composite targets," *Radio Sci.*, vol. 54, no. 8, pp. 785–807, 2019.



Tiziana Beltramonte was born in Benevento, Italy, in 1980. She received the M.S. (*summa cum laude*) degree in telecommunications engineering and the Ph.D. degree in information engineering from the Università degli Studi del Sannio, Benevento, Italy, in 2008 and 2012, respectively.

Since 2012, she has been with the Università degli Studi del Sannio, where she is currently a Research Fellow. Her research interests include satellite image processing and analysis, transmission data techniques, and global navigation satellite system reflectometry.



Paolo Braca (Senior Member, IEEE) received the Laurea (*summa cum laude*) degree in electronic engineering and the Ph.D. degree (highest rank) in information engineering from the University of Salerno, Fisciano, Italy, in 2006 and 2010, respectively.

In 2009, he was a Visiting Scholar with the Department of Electrical and Computer Engineering, University of Connecticut, Storrs, CT, USA. From 2010 to 2011, he was a Postdoctoral Associate with the University of Salerno, Italy. In 2011, he joined the NATO Science and Technology Organization Centre for Maritime Research and Experimentation, and is currently a Senior Scientist with the Research Department. As Project Manager, he has led the Data Knowledge Operational Effectiveness project, and several other research projects funded by the EU Horizon 2020, the US Office of Naval Research, and the Defence Research and Development Canada. In 2017 and 2018, he obtained the National Scientific Qualification to function as Associate and Full Professor in Italian Universities, respectively. In 2019, he was appointed as Adjunct Professor with the University of Cassino, Italy. He is the co-author of more than 100 publications in international scientific journals and conference proceedings. His research interests include statistical signal processing with emphasis on detection and estimation theory, wireless sensor network, multiagent algorithms, target tracking, data fusion, adaptation and learning over graphs, and radar (sonar) signal processing.

Dr. Braca is an Associate Editor of IEEE TRANSACTIONS ON SIGNAL PROCESSING, IEEE TRANSACTIONS ON AEROSPACE AND ELECTRONIC SYSTEMS, ISIF *Journal of Advances in Information Fusion*, EURASIP *Journal on Advances in Signal Processing*, and *IET Radar Sonar and Navigation*. In 2017, he was the Lead Guest Editor of the special issue "Sonar Multi-Sensor Applications and Techniques" in *IET Radar Sonar and Navigation*. He was an Associate Editor of *IEEE Signal Processing Magazine* (E-Newsletter) from 2014 to 2016. He is in the Technical Committee of the major international conferences in the field of signal processing and data fusion. He was the recipient of the Best Student Paper Award (first runner-up) at the 12th International Conference on Information Fusion in 2009. He received the NATO STO Scientific Achievement Award 2017 for his contribution to "Development and Demonstration of Networked Autonomous ASW" from the NATO Chief Scientist. He has coauthored the paper which was awarded with the Best Paper Award (first runner-up) at the Sensor Signal Processing for Defence 2019. He received the Premium Award for the best paper published on *IET Radar, Sonar and Navigation* in 2017–2019.



Maurizio Di Bisceglie (Member, IEEE) was born in Naples Italy. He received the Ph.D. degree in electronic and communications engineering from Università degli Studi di Napoli "Federico II," Naples, Italy, in 1993.

Since 1998, he is with Università degli Studi del Sannio, Benevento, as an Associate Professor of Telecommunications. He was a visiting scientist at the University College of London, London, U.K. and at the Defense Evaluation and Research Agency, Malvern, U.K. His research interests include the field

of statistical signal processing with applications to stochastic modeling and GNSS reflectometry.

Prof. Bisceglie was in the organizing committee of the Italian phase of EAQUATE (European AQUA Thermodynamic Experiment) mission, in 2004, Co-Chair of the NASA Direct Readout Conference, in 2005, and in the organizing committee of the IEEE 2008 Radar Conference. Since 2016, Maurizio di Bisceglie has been a member of the NASA CYGNSS external science team.



Alessio Di Simone (Member, IEEE) was born in Torre del Greco, Italy, in 1989. He received the B.Sc. and M.Sc. Laurea (*cum laude*) degrees in telecommunication engineering and the Ph.D. degree in information technology and electrical engineering from the University of Naples Federico II, Naples, Italy, in 2011, 2013, and 2017, respectively.

Since 2017, he has been a Research Fellow with the Department of Information Technology and Electrical Engineering, University of Naples Federico II. In 2016, he was a Visiting Researcher with the Universitat Politècnica de Catalunya, Barcelona, Spain. In 2017 and 2018, he was a Visiting Researcher with the NATO Science and Technology Organization Centre for Maritime Research and Experimentation (CMRE), La Spezia, Italy. His main research interests include the field of microwave remote sensing and electromagnetics including modeling of the electromagnetic scattering from natural surfaces, urban areas and artificial targets, simulation, and processing of SAR and GNSS-R data.

Dr. Di Simone was awarded a prize for the Best Master Thesis in Remote Sensing by the IEEE SOUTH ITALY GEOSCIENCE AND REMOTE SENSING CHAPTER in 2015.



Carmela Galdi (Member, IEEE) received the Dr.Eng. and Ph.D. degrees in electronic engineering from the Università degli Studi di Napoli Federico II, Naples, Italy, in 1992 and 1997, respectively.

In 1995, she spent a period for study and research in the Signal Processing Division, University of Strathclyde, Glasgow, U.K. In 1997, she was a Visiting Scientist at the University College of London, London, U.K., and at the Defense Evaluation and Research Agency, Malvern, U.K., working on statistical models of radar backscattering. In 2000, she joined the Università degli Studi del Sannio, Benevento, Italy, where she is currently an Associate Professor in Telecommunications. Her research interests include the field of statistical signal processing for remote sensing applications, non-Gaussian models of scattering from natural surfaces, and GNSS-R.

Prof. Galdi has cooperated with the National Oceanography Centre in Southampton, U.K., on a project about GNSS-R of the ocean surface. She is currently associated with the NASA CYGNSS project as external science team member.



Antonio Iodice (Senior Member, IEEE) was born in Naples, Italy, in 1968. He received the Laurea (*cum laude*) degree in electronic engineering and the Ph.D. degree in electronic engineering and computer science both from the University of Naples Federico II, Naples, Italy, in 1993 and 1999, respectively.

In 1995, he was with the Research Institute for Electromagnetism and Electronic Components of the Italian National Council of Research, Naples, Italy, and from 1999 to 2000 with Telespazio S.p.A., Rome, Italy. From 2000 to 2004, he was with the University of Naples Federico II as a Research Scientist and, from 2005 to 2018, as a Professor of Electromagnetics. He is currently a Full Professor of electromagnetics with the Department of Electrical Engineering and Information Technology of the University of Naples Federico II. He has been involved as Principal Investigator or Coinvestigator in several projects funded by European Union, Italian Space Agency, Italian Ministry of Education and Research, Campania Regional Government, and private companies. He has authored or coauthored more than 300 papers, of which more than 90 published on refereed journals. His main research interests include the field of microwave remote sensing and electromagnetics: Modeling of electromagnetic scattering from natural surfaces and urban areas, simulation and processing of synthetic aperture radar signals, and electromagnetic propagation in urban areas.

Prof. Iodice received the 2009 Sergei A. Schelkunoff Transactions Prize Paper Award from the IEEE Antennas and Propagation Society, for the best paper published in 2008 on the IEEE TRANSACTIONS ON ANTENNAS AND PROPAGATION. He was recognized by the IEEE Geoscience and Remote Sensing Society as a 2015 Best Reviewer of the IEEE TRANSACTIONS ON GEOSCIENCE AND REMOTE SENSING. He is the Chair of the IEEE South Italy Geoscience and Remote Sensing Chapter.



Leonardo M. Millefiori (Member, IEEE) received the B.Sc. degree in aerospace information engineering and the M.Sc. (*summa cum laude*) degree in communication engineering with a focus on the radar systems and remote sensing from the Sapienza University of Rome, Rome, Italy, in 2010 and 2013, respectively.

He was a visiting researcher with the NATO Science and Technology Organization Center for Maritime Research and Experimentation, La Spezia, where he joined the Research Department as research scientist in 2014. His research interests include target motion modeling, statistical learning and signal processing, and target tracking and data fusion.



Daniele Riccio (Fellow, IEEE) was born in Naples, Italy. He received the Laurea (*cum laude*) degree in electronic engineering from the University of Naples Federico II, Naples, Italy, in 1989.

He is a Full Professor of electromagnetic fields with the Department of Electrical Engineering and Information Technology. He also was a Research Scientist with the Italian National Research Council at the Institute for Research on Electromagnetics and Electronic Components (1989–1994), a Guest Scientist with the German Aerospace Centre (DLR), Munich, Germany (1994 and 1995), and a Research Affiliate to NASA, USA (2010–2018). He taught abroad as a lecturer to the Ph.D. programme with the Universitat Politècnica de Catalunya, Barcelona, Spain (2006) and with the Czech Technical University, Prague, Czech Republic (2012). He is a member of the Cassini Radar Science Team. He is the Coordinator of the Ph.D. Schools in Information and Communication Technology for Health and in Information Technology and Electrical Engineering at the University of Napoli Federico II, where he is the Representative within the Assembly of the National Inter-University Consortium for Telecommunications, and the Scientific Board of the Italian Society of Electromagnetism, where he is appointed with the Secretary role. He has authored three books, including *Scattering, Natural Surfaces*, and *Fractals* (Elsevier, 2007), and more than 400 scientific papers. His research interests include remote sensing, electromagnetic scattering from complex media and surfaces, synthetic aperture radar techniques, application of fractal geometry to remote sensing, propagation of electromagnetic fields for wireless communication networks.

Prof. Riccio is an Associate Editor for some journals on Remote Sensing. He was the General Chair of the *5G International Ph.D. School* in 2018 and 2019. He was the recipient of the 2009 Sergei A. Schelkunoff Transactions Prize Paper Award for the best paper published in 2008 on the IEEE TRANSACTIONS ON ANTENNAS AND PROPAGATION.



Peter Willett (Fellow, IEEE) received the B.A.Sc. degree from the University of Toronto, Toronto, ON, Canada, in 1982, and the Ph.D. degree from Princeton University, Princeton, NJ, in 1986.

He has been a Faculty Member with the Department of Electrical and Computer Engineering, the University of Connecticut, Storrs, CT, USA, since 1986. Since 1998, he has been a Professor. His research interests include statistical signal processing, detection, machine learning, communications, data fusion, and tracking.

Prof. Willett is a chief editor of *IEEE Aerospace and Electronic Systems (AESS) Magazine* (2018–2020). He was the Editor-in-Chief of *IEEE Signal Processing Letters*, 2014–2016 and before that for *IEEE TRANSACTIONS ON AEROSPACE AND ELECTRONIC SYSTEMS* from 2006 to 2011. He was also AESS Vice President for Publications 2012–2014. He is a member of the IEEE Fellows Committee, Ethics Committee, and Periodicals Committee, as well as the IEEE Signal Processing Society's Technical Activities and Conference Boards. He is the Chief Editor for the *IEEE AESS Magazine*. He is a member of the *IEEE AESS Board of Governors* and was a Chair of IEEE Signal Processing Society's Sensor-Array and Multichannel technical committee.